Materials Chemistry and Physics 252 (2020) 123213

Contents lists available at ScienceDirect

Materials Chemistry and Physics

journal homepage: www.elsevier.com/locate/matchemphys

Effect of combining with thermally expanded graphite on thermal conductivities of the lanthanum sulfate hydrate types of chemical heat storage material

Masashi Haruki *, Masayuki Fujita, Kouhei Takeda

Faculty of Mechanical Engineering, Institute of Science and Engineering, Kanazawa University, Kakuma-machi, Kanazawa, 920-1192, Japan

HIGHLIGHTS

- Hydration number of $La_2(SO_4)_3{\cdot}9H_2O$ did not change either at 35 or 60 °C for 120 min.
- TCs of pelletized $La_2(SO_4)_3{\cdot}xH_2O$ and β-$La_2(SO_4)_3{\cdot}xH_2O$/TEG were measured.
- TCs of both composites increased with increases in the content of TEG.
- TCs increased with increases in density regardless of the content of $La_2(SO_4)_3{\cdot}9H_2O$.

GRAPHICAL ABSTRACT

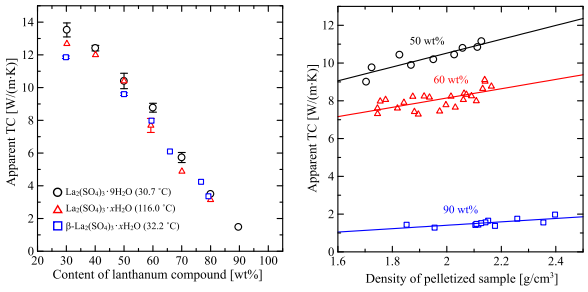

ARTICLE INFO

Keywords:
Thermal conductivity
Lanthanum sulfate hydrate
Thermally expanded graphite
Composite
Chemical heat storage

ABSTRACT

In the present work, the apparent thermal conductivities (TCs) parallel to the compaction direction of disk-like pelletized composites consisting of lanthanum sulfate hydrate ($La_2(SO_4)_3{\cdot}xH_2O$ ($x \leq 9$) and β-$La_2(SO_4)_3{\cdot}xH_2O$ ($x \leq 1$)) and thermally expanded graphite (TEG) were investigated to accumulate the fundamental thermophysical properties required to design a chemical heat-storage process that could recycle relatively low-temperature exhaust heat. The apparent TCs of both $La_2(SO_4)_3{\cdot}xH_2O$/TEG and β-$La_2(SO_4)_3{\cdot}xH_2O$/TEG were increased with increases in the content of TEG. Moreover, the apparent TCs were linearly increased with increases in the density regardless of the content of $La_2(SO_4)_3{\cdot}9H_2O$ at 50, 60 and 90 wt%. This density effect was possibly caused by a decrease in the interfacial thermal resistance between the interfaces of $La_2(SO_4)_3{\cdot}9H_2O$ - $La_2(SO_4)_3{\cdot}9H_2O$, TEG - TEG and $La_2(SO_4)_3{\cdot}9H_2O$ - TEG grain pairs when the crimping force was enhanced due to increase in the density.

1. Introduction

Global warming and resource depletion are serious issues that must be resolved as soon as possible. Heat storage techniques are among the most promising methods for the effective utilization of energy, and many studies into sensible heat storage, latent heat storage, and chemical heat storage have been reported thus far [1–3]. Among them, chemical heat storage that is based on reversible chemical reactions such as dehydration/hydration between the hydroxide and the oxide of alkaline earth metals such as $Mg(OH)_2$/MgO and $Ca(OH)_2$/CaO have gained attention because of a higher level of heat-storage density and long-term heat storage ability [4–6].

* Corresponding author.
E-mail address: mharuki@se.kanazawa-u.ac.jp (M. Haruki).

https://doi.org/10.1016/j.matchemphys.2020.123213
Received 23 March 2020; Received in revised form 7 May 2020; Accepted 10 May 2020
Available online 20 May 2020

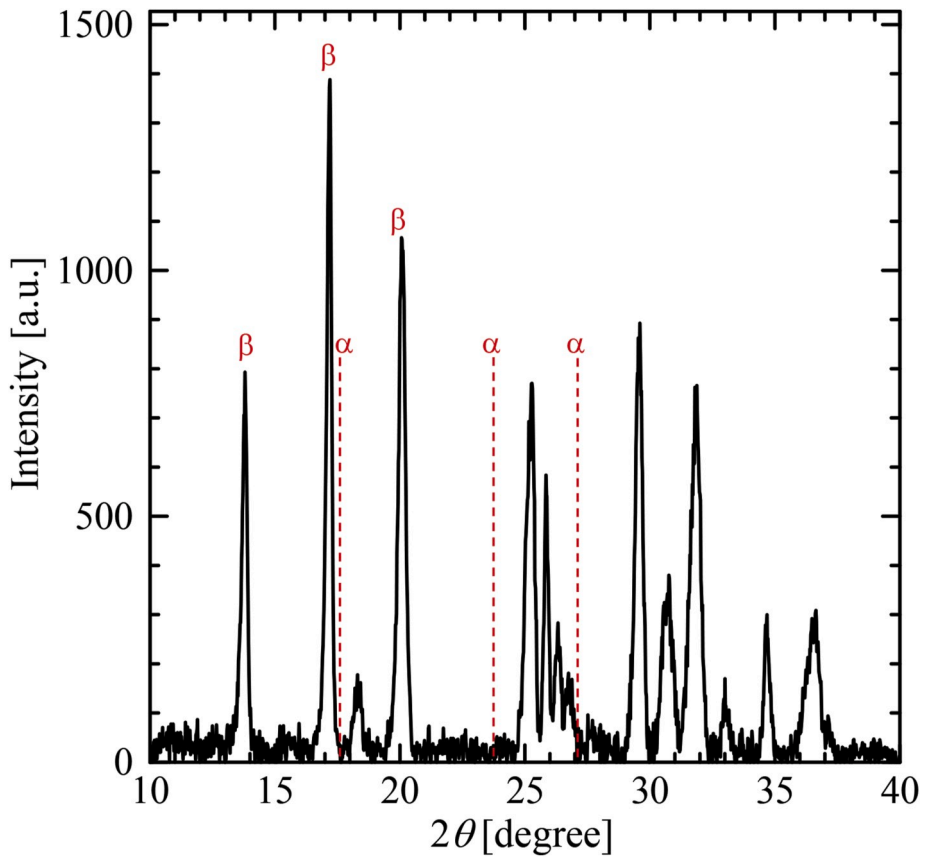

Fig. 1. XRD pattern of the sample obtained after dehydration of $La_2(SO_4)_3 \cdot 9H_2O$ at 570 °C for 60 min. α and β show the characteristic angles of α-$La_2(SO_4)_3$ and β-$La_2(SO_4)_3$ referred from the literature [7].

Recently, a reversible reaction between the dehydration of β-lanthanum sulfate monohydrate (β-$La_2(SO_4)_3 \cdot H_2O$) and the hydration of β-lanthanum sulfate (β-$La_2(SO_4)_3$) was reported as a promising chemical heat storage reaction for the recycling of low-grade exhaust heat at temperatures lower than 250 °C [7–9]. The reaction scheme for heat storage and release is shown by Eq. (1).

$$\beta\text{-}La_2(SO_4)_3 \cdot H_2O\ (s) \rightleftarrows \beta\text{-}La_2(SO_4)_3\ (s) + H_2O\ (g),\ \Delta H^o = 91\ \text{kJ/mol} \quad (1)$$

This reaction features a hydration rate from β-$La_2(SO_4)_3$ to β-$La_2(SO_4)_3 \cdot H_2O$ that is relatively high. Moreover, the hydration reaction is expected to proceed even at temperatures that approximate the dehydration temperature because the thermal hysteresis between the hydration and dehydration curves is small [9]. The physicochemical and structural characteristics of those materials have been well studied. Therefore, investigations and accumulations of the fundamental engineering data are expected to be the next step for the material design and practical use.

For the practical use of ceramics as chemical heat storage materials, thermal conductivity (TC) should be improved because the reaction rate and chemical equilibrium constant depend on the temperature, and prompt heat transfer is also required for efficient heat release. As for the electrical and magnetic properties, doping with additional metal ions [10] and controlling the oxygen degree of the cation [11] have often been applied to change the properties of the materials. Moreover, techniques to improve the function of ceramic materials such as the addition of functional carbons and metals has also been common in fields concerned with magnetic properties [12,13]. The latter techniques have often been applied to heat-storage materials to enhance the TC. The TCs of chemical heat storage materials such as $Mg(OH)_2$ and MgO have been improved by mixing them with thermally expanded graphite (TEG). Also, the influences that the content of TEG and the sample density exert on the TC of the composite blocks of $Mg(OH)_2$/TEG and MgO/TEG have been investigated [14,15]. Moreover, the relationship between the apparent TCs of the pelletized composite materials of both $Mg(OH)_2$/TEG and MgO/TEG and the compositions of $Mg(OH)_2$ and MgO in the composites, were also investigated across a wide range of the compositions in our previous study [16]. As for the field of hydrogen storage application, expanded natural graphite was also added to the Mg_{90}–Ni_{10} alloy to prepare the composite material for enhancement of the TC of the Mg_{90}–Ni_{10} alloy [17].

The present work was focused on TEG as a thermally conductive material, and the effect that the addition of the TEG exerted on the TCs of $La_2(SO_4)_3 \cdot xH_2O$ ($x \leq 9$) and β-$La_2(SO_4)_3 \cdot xH_2O$ ($x \leq 1$) was investigated to accumulate fundamental data for the design of a heat storage process that could recycle low-temperature exhaust heat (<250 °C). The relationships between the content of TEG and the apparent TCs were first examined. Then the effects that grain size and the density of the composite samples exerted on the apparent TCs were investigated in order to determine the methods for increasing the TC of the composite materials under a constant content of TEG because the increment of the content of TEG that is replaced by the heat storage material leads to a reduction in heat-storage density.

2. Experiment

2.1. Materials

Lanthanum sulfate nonahydrate ($La_2(SO_4)_3 \cdot 9H_2O$) with purity >99.9% was purchased from FUJIFILM Wako Pure Chemical Co. and was used as a lanthanum sulfate material without further purification. Thermally expandable graphite (SS-3 grade) was supplied from Air Water Co., and it was thermally expanded under a nitrogen atmosphere

in an electric furnace at 670 °C for 60 min to obtain TEG.

The pelletized composite materials of $La_2(SO_4)_3{\cdot}9H_2O$/TEG were used to determine their apparent TCs. To prepare the pelletized samples, $La_2(SO_4)_3{\cdot}9H_2O$ and TEG were mixed using a grinder mill (Iwatani Co. Crush Millser) for approximately 60 s except for investigation into the material grain size effect, and the powdery mixture was pelletized into a disk-like shape using an oil-hydraulic-press compression machine. The diameter of the samples was set at 2 cm, and the thickness was set at approximately 1.7 mm with the exception of the investigation into the effect of sample thickness. The compression pressures loading to the samples approximately ranged from 25 to 250 MPa depending on the objective sample density. Disk-shaped sample could not be obtained when only $La_2(SO_4)_3$ was compressed, which seemed to indicate TEG also played the role of binder. The morphology of the composite samples was analyzed using a scanning electron microscope (SEM, JEOL Co., JSM-7100). Observation surfaces were coated with a gold (60%) and palladium (40%) alloy via ion sputter (Hitachi Co., E−1030) prior to the SEM observation. The sizes of the grains of the $La_2(SO_4)_3{\cdot}9H_2O$ and TEG were analyzed using Image J software. Moreover, the weight percent of $La_2(SO_4)_3{\cdot}xH_2O$ in the pelletized composite samples was estimated on the assumption that all $La_2(SO_4)_3{\cdot}xH_2O$ compounds were $La_2(SO_4)_3{\cdot}9H_2O$, and the apparent TCs were measured at a weight percent of $La_2(SO_4)_3{\cdot}9H_2O$ that ranged from 30 to 90 wt% in the present work.

β-$La_2(SO_4)_3$ was prepared by heating $La_2(SO_4)_3{\cdot}9H_2O$ under a nitrogen atmosphere at 570 °C for 60 min according to a reference to data found in the literature [7]. The crystalline structure of the obtained β-$La_2(SO_4)_3$ was analyzed via X-ray diffractometer (XRD, Rigaku Co., MiniFlex II). The XRD pattern of the prepared β-$La_2(SO_4)_3$ is shown in Fig. 1. Peaks indicating the existence of β-$La_2(SO_4)_3$ crystalline structures were found on the spectrum. On the other hand, peaks that could clearly be assigned to the structure of α-$La_2(SO_4)_3$ could not be found.

2.2. Measurement of the relationship between the temperature and the hydration number of $La_2(SO_4)_3{\cdot}xH_2O$

Before measurement of the apparent TCs of the $La_2(SO_4)_3{\cdot}xH_2O$/TEG composites, the temperature dependency of the hydration number of $La_2(SO_4)_3{\cdot}xH_2O$ was checked at temperatures ranging from 35 to 200 °C. In the measurement, a certain weight of $La_2(SO_4)_3{\cdot}9H_2O$ was heated at each temperature using a thermostatic air bath, and the chronological changes in the weight were measured. Eq. (2) was used to convert the weight changes into a hydration number.

$$x(t) = 9 - \frac{W(0) - W(t)}{M_{H2O}\frac{W(0)}{M_{La}}} \tag{2}$$

In Eq. (2), $x(t)$ indicates the hydration number at elapsed-time, t, from the beginning of the heating. $W(0)$ and $W(t)$ show the weights of $La_2(SO_4)_3{\cdot}xH_2O$ at the initial state and time, t, respectively. M_{H2O} and M_{La} represent the molecular weights of water and $La_2(SO_4)_3{\cdot}9H_2O$, respectively.

2.3. Measurement of apparent TCs

The apparent TCs in the compressive direction for the disk-like pelletized $La_2(SO_4)_3{\cdot}xH_2O$/TEG composites were measured using an in-house apparatus based on a temperature gradient steady-state method. The apparatus was developed in our previous work [16] and details of the apparatus and measurements are shown there. Therefore, only a brief explanation is provided here. The TC meter used consisted of two cylindrical tough-pitch copper rods that were both 20 mm in diameter, a band heater (Sakaguchi E.H VOC Co., MB1A1JN2) used as a heat source, and a water bath used as a heat sink. Copper rods 150 and 250 mm in length served as the upper and bottom sides, respectively, and were thermally insulated using foamed silicone. In measurements,

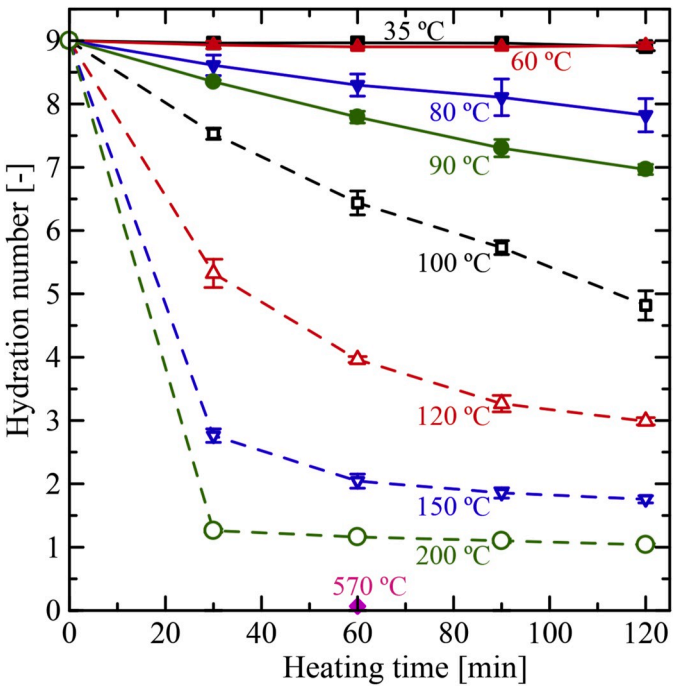

Fig. 2. Relationship between the heating temperature and time and the hydration number of $La_2(SO_4)_3{\cdot}9H_2O$. Starting material was $La_2(SO_4)_3{\cdot}9H_2O$.

the sample was sandwiched between two copper rods. Heat was supplied to the edge of the upper copper rod via a band heater at a constant AC voltage. The temperatures of the two copper rods were measured at 5 points each by thermocouples to estimate the heat flux penetrating the composite sample. The heat flux, q, was obtained by the fist-order thermal conduction of Fourier's law, as shown by Eq. (3).

$$q = -k_{Cu}\frac{dT}{dx} \tag{3}$$

In Eq. (3), k_{Cu} indicates the TC for the tough-pitch copper of 381 W/(m·K). The temperature gradient in the copper rods, dT/dx, was obtained from the 5-point temperature measurements of each rod. The total thermal resistance for the measurement of the apparent TC is shown as the ratio of the temperature difference between both sample surfaces where they contact each copper rod and the heat flux obtained using Eq. (3). The total resistance, R_t, is estimated as shown in Eq. (4).

$$R_t = \frac{\Delta T_S}{q} = R_S + R_i \tag{4}$$

In Eq. (4), ΔT_S is the temperature difference between both sample surfaces. R_S and R_i show the thermal resistances caused by the sample and the interfacial resistances between the sample and the rods, respectively. R_S also represents the ratio of the sample thickness to the TC of the sample. Therefore, Eq. (4) is converted to Eq. (5).

$$\frac{\Delta T_S}{q} = R_S + R_i = \frac{t_S}{k_S} + R_i \tag{5}$$

In Eq. (5), t_S and k_S indicate the sample thickness and the TC of the sample, respectively. The linear relationship was expected to obtain for the relationship between the sample thickness and the total thermal resistance, as demonstrated by the slope and the intercept of $1/k_S$ and R_i, respectively. According to the literature [18,19], the apparent TCs, k_{eff}, were determined by measurements at similar sample thicknesses of 1.7 mm using Eq. (6) for convenience in the present work.

$$k_{eff} \approx q\frac{ts}{\Delta T_S} \tag{6}$$

The apparent TCs include the influence of the interfacial thermal

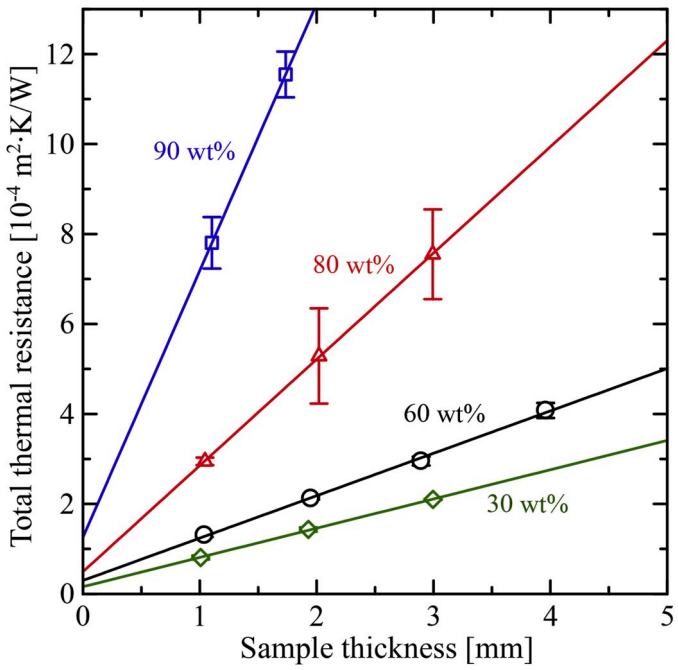

Fig. 3. Relationship between the sample thickness and the total thermal resistance for the measurement of $La_2(SO_4)_3 \cdot 9H_2O$/TEG sample at the sample temperatures of around 31.0 °C.

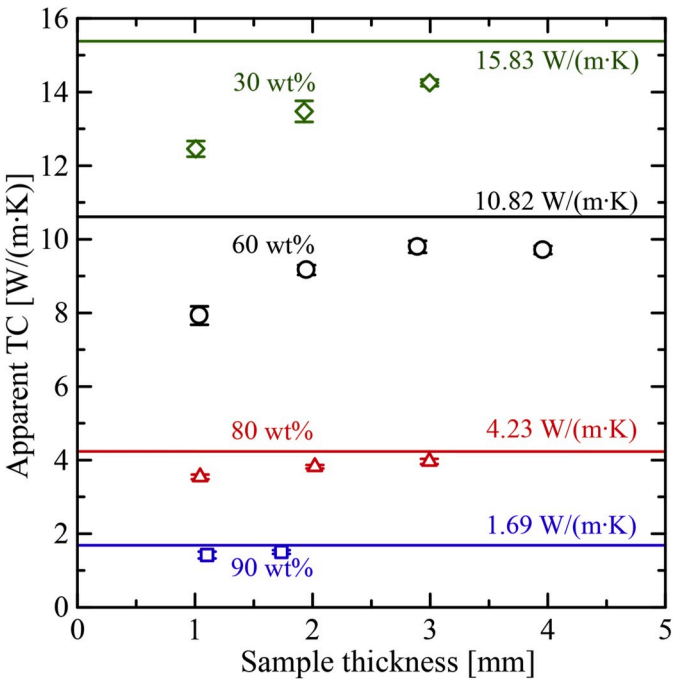

Fig. 4. Dependency of the apparent TCs on the sample thickness for $La_2(SO_4)_3 \cdot 9H_2O$/TEG composite samples at the sample temperatures of around 31.0 °C. Lines show the TCs obtained from the results shown in Fig. 3 and Eq. (5).

resistance that exists on both surfaces of the sample. This influence is discussed in the following Results and Discussion section.

3. Results and discussion

3.1. Temperature dependency of the hydration number of $La_2(SO_4)_3 \cdot xH_2O$

According to the literature [7], $La_2(SO_4)_3 \cdot 9H_2O$ becomes an amorphous state at around 200 °C, and changes to crystalline β-$La_2(SO_4)_3$ at around 300 °C. β-$La_2(SO_4)_3$ then changes to a monoclinic polymorph crystalline of α-$La_2(SO_4)_3$ at a temperature higher than 600 °C. β-$La_2(SO_4)_3$ can form β-$La_2(SO_4)_3 \cdot xH_2O$ ($0 \leq x \leq 1$) under humidified conditions, but water insertion can not be found in the crystal structure of α-$La_2(SO_4)_3$. First, the temperature and time dependency of the hydration number was investigated. The relationships between temperature and changes in the levels of hydration under an air atmosphere are shown in Fig. 2. The hydration number was obtained using Eq. (2). No changes in hydration were observed for $La_2(SO_4)_3 \cdot 9H_2O$ at 35 and 60 °C even after 120 min. On the other hand, a reduction in the hydration number was observed and the degree of the reduction was increased with increasing temperature at more than 80 °C. The hydration number reached 1 at 200 °C. When $La_2(SO_4)_3 \cdot 9H_2O$ was heated at 570 °C for 60 min under a nitrogen atmosphere, the hydration number was approximately zero, at which point β-$La_2(SO_4)_3$ should have been produced based on the XRD pattern shown in Fig. 1. This result also indicated the assumption of the initial hydration number of 9 was reasonable.

3.2. Measurements of apparent TCs

3.2.1. Relationship between the composition, temperature and apparent TCs of $La_2(SO_4)_3 \cdot xH_2O$ and β-$La_2(SO_4)_3 \cdot xH_2O$

First, the relationships between the sample thickness and the apparent TCs were investigated to confirm the appropriateness of discussions based on the apparent TCs obtained by Eq. (6). The relationships between the sample thickness and the total thermal resistance are shown in Fig. 3. The sample temperature that was defined as the average

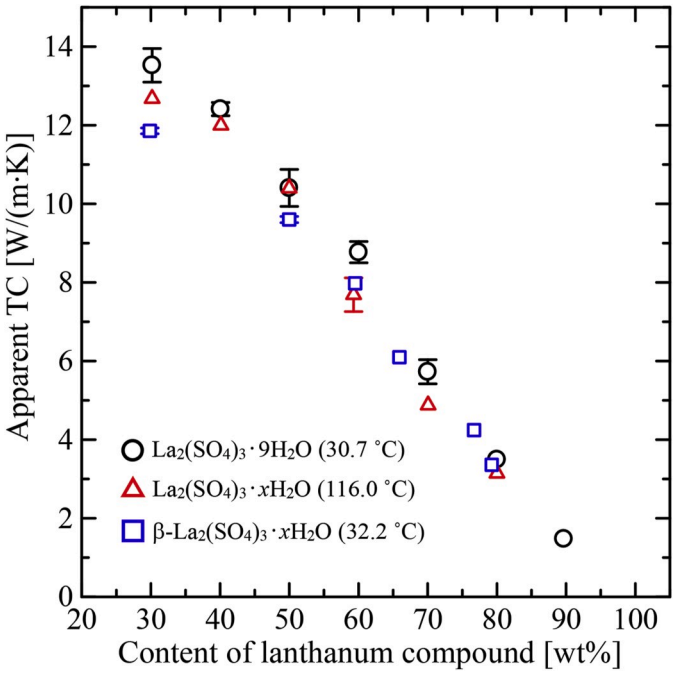

Fig. 5. Relationships between the lanthanum compound content and the apparent TCs for $La_2(SO_4)_3 \cdot xH_2O$/TEG and β- $La_2(SO_4)_3 \cdot xH_2O$/TEG composite samples.

temperature of both surfaces of the disk-like samples was 31.0 ± 2.6 °C. According to the results shown in Fig. 2, the hydration numbers of $La_2(SO_4)_3 \cdot xH_2O$ should remain 9 during measurements. The deviations of the total thermal resistances for the 80 and 90 wt% $La_2(SO_4)_3 \cdot 9H_2O$ were much larger than those at 30 and 60 wt%. One of the possible reasons for this deviation behavior is that the reproducibility of the

Table 1
Grain size data for TEG used.

	s60-1-TEG	s60-2-TEG	s60-3-TEG	s60-4-TEG	s90-1-TEG	s90-2-TEG
Content of $La_2(SO_4)_3 \cdot 9H_2O$ [wt %]	60	60	60	60	90	90
Crush and mixing time [min]	1	2	3	4	1	2
Number of grains measured	551	354	426	554	315	200
Average longer diameter [μm]	264	155	132	138	266	88
Max. longer diameter [μm]	736	473	571	492	680	413
Min. longer diameter [μm]	55	55	44	42	67	27
STD[a] [μm]	116	72.6	69.9	70.5	128	54.6
CV[b] value [%]	44	47	53	51	48	62

[a] Standard deviation.
[b] Coefficient of variation: 100 × STD/Average longer diameter [%].

Table 2
Grain size data for $La_2(SO_4)_3 \cdot 9H_2O$ used.

	s60-1-La	s60-2-La	s60-3-La	s60-4-La	s90-1-La	s90-2-La
Content of $La_2(SO_4)_3 \cdot 9H_2O$ [wt %]	60	60	60	60	90	90
Crush and mixing time [min]	1	2	3	4	1	2
Number of grains measured	1809	2440	1934	2000	1759	3086
Average longer diameter [μm]	18.6	17.6	17.5	16.8	16.9	15.1
Max. longer diameter [μm]	74	83	80	88	80	82
Min. longer diameter [μm]	3	3	3	3	2	2
STD[a] [μm]	10.8	10.1	9.6	8.6	10.7	9.6
CV value[b] [%]	58	57	55	52	64	64

[a] Standard deviation.
[b] Coefficient of variation: 100 × STD/Average longer diameter [%].

contacting behaviors of $La_2(SO_4)_3 \cdot 9H_2O$ - $La_2(SO_4)_3 \cdot 9H_2O$ grains may be lower than those between $La_2(SO_4)_3 \cdot 9H_2O$ - TEG grains due to the hardness of the $La_2(SO_4)_3 \cdot 9H_2O$ grains. As shown in Fig. 3, linear relationships were obtained regardless of the $La_2(SO_4)_3 \cdot 9H_2O$ compositions at 30, 60, 80, and 90 wt%. Therefore, the TCs of the samples were obtained using Eq. (5) as the reciprocals of the slopes of the linear relationships obtained in Fig. 3 at each composition, and both the apparent TCs and the TCs that were obtained by Eq. (6) and Eq. (5), respectively, are shown in Fig. 4. The apparent TCs were slightly increased with increases in the sample thickness regardless of $La_2(SO_4)_3 \cdot 9H_2O$ content in the pelletized samples. The values of the apparent TCs were slightly lower than those of the TCs obtained by Eq. (5) due mainly to the influence of the interfacial resistance, as mentioned above. The deviations between the apparent TCs of the samples with 1.7–2.0 mm thicknesses and the estimated TCs were below approximately 15%, and we considered that using the apparent TCs of the samples with 1.7–2.0 mm would be reasonable for the discussion below.

The relationships between the weight percent of $La_2(SO_4)_3 \cdot xH_2O$ and the apparent TCs at the sample temperatures of 30.7 ± 2.3 and 116.0 ± 1.6 °C are shown in Fig. 5. Based on the results of the measurements of the hydration number shown in Fig. 2, the data at around 30.7 °C should be the apparent TCs of $La_2(SO_4)_3 \cdot 9H_2O$/TEG composites. On the other hand, the apparent TCs measured at around 116.0 °C should be assigned to $La_2(SO_4)_3 \cdot xH_2O$ ($x \leq 9$) because dehydration should have proceeded during the measurements. Both of these apparent TCs monotonically decreased with increases in the weight percent of $La_2(SO_4)_3 \cdot xH_2O$ ranging from 30 to 90 wt%. The apparent TC at 116.0 °C was marginally lower than that at 30.7 °C. Moreover, the apparent TCs of the β-$La_2(SO_4)_3 \cdot xH_2O$/TEG ($x \leq 1$) at sample temperatures of 32.2 ± 5.6 °C are also described in Fig. 5. As shown in the figure, the apparent TCs of β-$La_2(SO_4)_3 \cdot xH_2O$/TEG indicated values similar to those of $La_2(SO_4)_3 \cdot xH_2O$/TEG. Although the TCs of pure $La_2(SO_4)_3 \cdot xH_2O$ and β-$La_2(SO_4)_3 \cdot xH_2O$ were not clarified, the effect of the difference in the crystalline structure could not be clearly seen even by mixing with only 20 wt% TEG. Functional carbon was also used to control the magnetic properties of the composite materials with a small addition amount, and the magnetic hysteresis curve and anisotropy of barium ferrite/epoxy resin composites could be varied by the addition of multi-walled carbon nanotubes and graphene nanoplatelets even at 5 wt% [12].

3.2.2. *Effect of the grain size of TEG and the sample density on the apparent TCs*

The effect that the grain size of TEG exerted on the apparent TCs of $La_2(SO_4)_3 \cdot 9H_2O$/TEG were examined at 60 and 90 wt% of

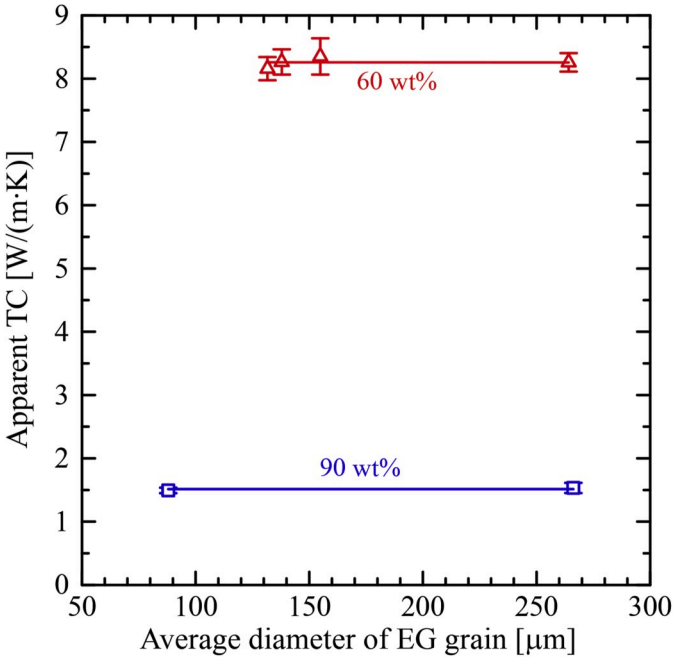

Fig. 6. Relationship between the average grain sizes of TEG and the apparent TCs for $La_2(SO_4)_3 \cdot 9H_2O$/TEG pelletized sample at the sample temperatures of around 31.6 °C.

$La_2(SO_4)_3 \cdot 9H_2O$. The grain size of TEG was adjusted by changing the time of the crush and mixing processes via the grinder mill. The grain size distributions of TEG and $La_2(SO_4)_3 \cdot 9H_2O$ are shown in Figs. S1 and S2, respectively, and the average values and deviations are also listed in Tables 1 and 2, respectively. The average grain size of $La_2(SO_4)_3 \cdot 9H_2O$ was not drastically changed during the crush and mixing processes in time from 60 to 240 s although some fluctuation was detected in the distribution. On the other hand, changes in both the average value and in the distribution were found for the TEG grains. In the literature [20, 21], the affect that grain size exerted on the characteristics of the crystalline structure ultimately affected the properties of the functional ceramics. The average sizes of $La_2(SO_4)_3 \cdot 9H_2O$ used had close values that were relatively large (15–19 μm). The difference in results between lots should not include the influence of the small difference in the size of $La_2(SO_4)_3 \cdot 9H_2O$. The relationships between the grain size of TEG and the apparent TC at the sample temperatures of 31.6 ± 3.2 °C are shown

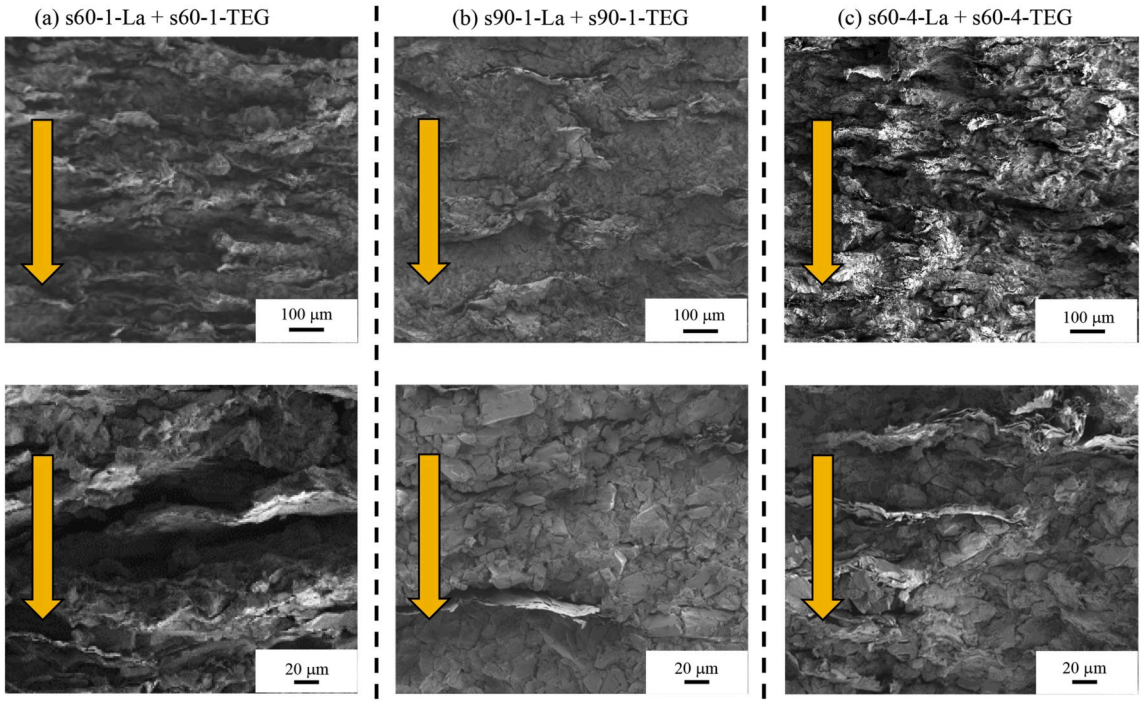

Fig. 7. SEM images of cross-sections of $La_2(SO_4)_3 \cdot 9H_2O$/TEG at 60 and 90 wt% of $La_2(SO_4)_3 \cdot 9H_2O$. Bottom side images are enlarged versions, and arrows indicate the compressive direction at the sample preparation. Information of grains of each composite are listed in Tables 1 and 2 for TEG and $La_2(SO_4)_3 \cdot 9H_2O$, respectively.

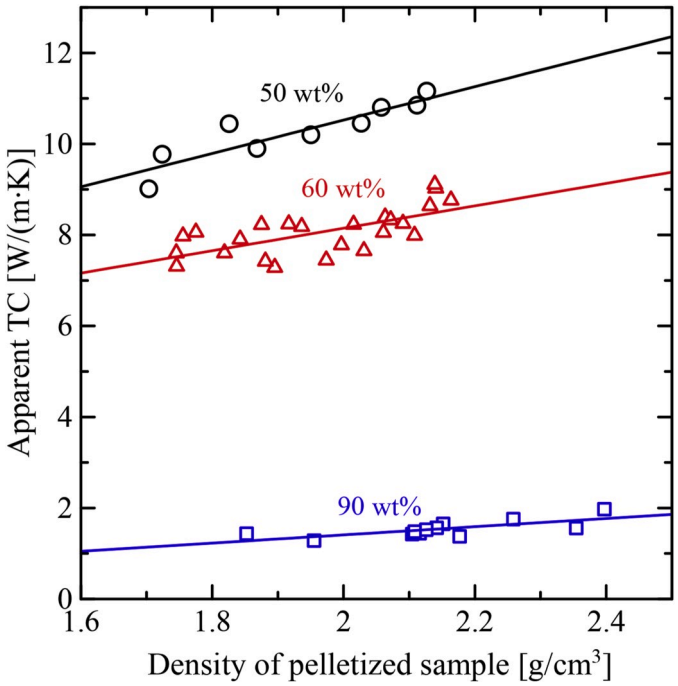

Fig. 8. Dependency of the apparent TC on the sample density for $La_2(SO_4)_3 \cdot 9H_2O$/TEG pelletized sample at the sample temperatures of around 30.8 °C.

in Fig. 6. For the average grain size of TEG ranging from 90 to 270 μm, the dependency of the apparent TC on the grain size was not found for $La_2(SO_4)_3 \cdot 9H_2O$ content of either 60 or 90 wt%. SEM images of the cross-sections of the pelletized samples of the $La_2(SO_4)_3 \cdot 9H_2O$/TEG at 60 and 90 wt% of $La_2(SO_4)_3 \cdot 9H_2O$ are shown in Fig. 7. As shown in the figure, the layered structures of TEGs were observed in the cross-sectional SEM images of the composite samples regardless of the TEG grain size. One possible reason why the apparent TCs did not depend on the grain size of the TEG may have been that the layered structures of TEG grains were approximately perpendicular to the out-of-plain direction of the pelletized sample.

To study the effect of the sample density on the apparent TCs, the densities of the samples were varied by adjustment of the sample amount and by the compressive load during the preparation of the pelletized samples. The average TEG grain sizes were estimated at approximately 260 μm, as shown in Table 1. The relationships between the sample densities and the apparent TCs of $La_2(SO_4)_3 \cdot 9H_2O$ at 50, 60 and 90 wt% and at the sample temperatures of 30.8 ± 3.2 °C are shown in Fig. 8. The apparent TCs increased with increasing density regardless of the content of $La_2(SO_4)_3 \cdot 9H_2O$, and this trend was also observed for the $Mg(OH)_2$/TEG composite material in the previous work [15]. This increment would be caused by reductions in the interfacial thermal resistances between the interfaces of $La_2(SO_4)_3 \cdot 9H_2O$ - $La_2(SO_4)_3 \cdot 9H_2O$, TEG - TEG and $La_2(SO_4)_3 \cdot 9H_2O$ - TEG grain pairs due to an enhancement of the crimping force. If water vapor can permeate these high-density matrices during both heat storage and release operations, compaction of the samples would become an important operation from the view points of both the thermal conductivity and heat-storage density. In future work, the hydration and dehydration reaction rate of this composite material will be evaluated using high-density samples.

4. Conclusions

In the present work, the apparent TCs in the compressive directions of $La_2(SO_4)_3 \cdot xH_2O$/TEG ($x \leq 9$) and β-$La_2(SO_4)_3 \cdot xH_2O$/TEG ($x \leq 1$) were investigated to clarify the effect that TEG exerts on the TCs for practical use. These materials have recently been reported as promising heat-storage candidates for the recovery of exhaust heat at temperatures lower than 250 °C. The apparent TCs increased with increases in the TEG content in the pelletized sample. As for the relationship between the TEG content and the apparent TC, no obvious differences could be found in the results between $La_2(SO_4)_3 \cdot 9H_2O$/TEG and β-$La_2(SO_4)_3 \cdot xH_2O$/TEG. Furthermore, the apparent TCs of $La_2(SO_4)_3 \cdot 9H_2O$/TEG did not depend on the grain sizes of the TEG samples when the average sizes ranged

from approximately 90 to 270 μm. On the other hand, the apparent TCs were approximately linearly increased with increases in the density of the pelletized composite samples.

Declaration of competing interest

The authors declare that they have no known competing financial interests or personal relationships that could have appeared to influence the work reported in this paper.

CRediT authorship contribution statement

Masashi Haruki: Conceptualization, Methodology, Validation, Formal analysis, Investigation, Writing - original draft, Writing - review & editing, Funding acquisition. **Masayuki Fujita:** Validation, Investigation, Writing - review & editing. **Kouhei Takeda:** Validation, Investigation, Writing - review & editing.

Acknowledgement

The authors sincerely appreciate the Fuji Science and Technology Foundation for financial support of a portion of this work.

Appendix A. Supplementary data

Supplementary data to this article can be found online at https://doi.org/10.1016/j.matchemphys.2020.123213.

References

[1] H. Zhang, J. Baeyens, G. Cáceres, J. Degrève, Y. Lv, Thermal energy storage: recent developments and practical aspects, Prog. Energy Combust. Sci. 53 (2016) 1–40.
[2] O. Achkari, A.E. Fadar, Latest developments on TES and CSP technologies - energy and environmental issues, applications and research trends, Appl. Therm. Eng. 167 (2020) 114806.
[3] C. Suresh, R. P. Saini, Review on solar thermal energy storage technologies and their geometrical configurations, Int. J. Energy Res. In press, https://doi.org/10.1002/er.5143.
[4] P. Pardo, A. Deydier, Z. Anxionnaz-Minvielle, S. Rougé, M. Cabassud, P. Cognet, A review on high temperature thermochemical heat energy storage, Renew. Sustain. Energy Rev. 32 (2014) 591–610.
[5] T. Yan, R.Z. Wang, T.X. Li, L.W. Wang, I.T. Fred, A review of promising candidate reactions for chemical heat storage, Renew. Sustain. Energy Rev. 43 (2015) 13–31.
[6] X. Chen, Z. Zhang, C. Qi, X. Ling, H. Peng, State of the art on the high-temperature thermochemical energy storage systems, Energy Covers, Manage 177 (2018) 792–815.
[7] N. Hatada, K. Shizume, T. Uda, Discovery of rapid and reversible water insertion in rare earth sulfates: a new process for thermochemical heat storage, Adv. Mater. 29 (2017) 1606569.
[8] K. Toyoura, H. Tai, N. Hatada, K. Shizume, T. Uda, One-dimensional water channels in lanthanum sulfate: a first-principles study, J. Mater. Chem. A 5 (2017) 20188–20194.
[9] K. Shizume, N. Hatada, K. Toyoura, T. Uda, Characteristic microstructure underlying the fast hydration–dehydration reaction of β-$La_2(SO4)_3$: “fine platy joints” with “loose grain boundaries”, J. Mater. Chem. A 6 (2018) 24956–24964.
[10] M.V. Zdorovetsa, A.L. Kozlovskiy, Study of the effect of La^{3+} doping on the properties of ceramics based on $BaTiO_x$, Vacuum 168 (2019) 108838.
[11] S.V. Trukhanov, L.S. Lobanovski, M.V. Bushinsky, I.O. Troyanchuk, H. Szymczak, Magnetic phase transitions in the anion-deficient $La_{1-x}Ba_xMnO_{3-x/2}$ ($0 \le x \le 0.50$) manganites, J. Phys. Condens. Matter 15 (2003) 1783–1795.
[12] O.S. Yakovenko, L.Y. Matzui, L.L. Vovchenko, A.V. Trukhanov, I.S. Kazakevich, S. V. Trukhanov, Y.I. Prylutskyy, U. Ritter, Magnetic anisotropy of the graphite nanoplatelet-epoxy and MWCNT-epoxy composites with aligned barium ferrite filler, J. Mater. Sci. 52 (2017) 5345–5358.
[13] L.Y. Matzui, A.V. Trukhanov, O.S. Yakovenko, L.L. Vovchenko, V.V. Zagorodnii, V. V. Oliynyk, M.O. Borovoy, E.L. Trukhanova, K.A. Astapovich, D.V. Karpinsky, S. V. Trukhanov, Functional magnetic composites based on hexaferrites: correlation of the composition, magnetic and high-frequency properties, Nanomaterials 9 (2019) 1720.
[14] O. Myagmarjav, M. Zamengo, J. Ryu, Y. Kato, Energy density enhancement of chemical heat storage material for magnesium oxide/water chemical heat pump, Appl. Therm. Eng. 91 (2015) 377–386.
[15] M. Zamengo, J. Tomaškovič, J. Ryu, Y. Kato, Thermal conductivity measurements of expanded graphite - magnesium hydroxide composites for packed bed reactors of chemical heat storage/pump systms, J. Chem. Eng. Jpn. 49 (2016) 261–267.
[16] M. Haruki, K. Saito, K. Takai, M. Fujita, H. Onishi, Y. Tada, Thermal conductivity and reactivity of $Mg(OH)_2$ and MgO/expanded graphite composites with high packing density for chemical heat storage, Thermochim. Acta 680 (2019) 178338.
[17] C. Pohlmann, L. Röntzsch, S. Kalinichenka, T. Hutsch, T. Weißgärber, B. Kieback, Hydrogen storage properties of compacts of melt-spun $Mg_{90}Ni_{10}$ flakes and expanded natural graphite, J. Alloys Compd. 509S (2011) S625–S628.
[18] T. Ogushi, S. Yanaura, S. Watanabe, T. Hirata, Thermal conductivity measurement method for isotropic conductive adhesives, Netsu Bussei 28 (2014) 22–28.
[19] M. Haruki, J. Tada, K. Tanaka, H. Onishi, Y. Tada, Enhancing the effective thermal conductivity of Kapton-type polyimide sheets via the use of hexagonal boron nitride, Thermochim. Acta 662 (2018) 1–7.
[20] S.V. Trukhanov, A.V. Trukhanov, H. Szymczak, C.E. Botez, A. Adair, Magnetotransport properties and mechanism of the A-site ordering in the Nd–Ba optimal-doped manganites, J. Low Temp. Phys. 149 (2007) 185–199.
[21] M.V. Zdorovets, A. Arbuzd, A.L. Kozlovskiy, Synthesis of $LiBaZrO_x$ ceramics with a core-shell structure, Ceram. Int. 46 (2020) 6217–6221.